



Original Article

Shrinkage and dimensional accuracy of porous ceramics derived from capillary suspensions

Moritz Weiß^{a,b,*}, Johannes Maurath^b, Norbert Willenbacher^b, Erin Koos^a^a KU Leuven, Department of Chemical Engineering, B-3001 Leuven, Belgium^b Karlsruhe Institute of Technology, Institute for Mechanical Process Engineering and Mechanics, 76131 Karlsruhe, Germany

ARTICLE INFO

Keywords:

Capillary suspensions
Open porous ceramics
Shrinkage
Net-shape accuracy
Extrusion

ABSTRACT

Shrinkage and dimensional accuracy are of particular importance for industrial material production. High dimensional accuracy directly lowers finishing works and cost. Capillary suspension processing is a novel, easy method to produce highly porous ceramic materials. Their shrinkage and shape accuracy is investigated during processing using a laser microscope. The total shrinkage is reduced by 20% for capillary suspension compared to pure suspension. This results from an increase in linear shape accuracy for top radii as well as height. The linear shape accuracy is increased by 6% in top radius and by 16% in height by using the capillary suspension phenomenon. We also show that this capillary suspension method is applicable for continuous shaping processes, like extrusion. The combination of an easy, robust processing route with known dimensional accuracy and applicability for continuous shaping processes makes this capillary suspension processing route highly desirable for industrial processes.

1. Introduction

Fabrication of dimensionally accurate ceramic components is of particular importance in industrial manufacturing [1–6]. Dimensional accuracy is normally realized through machining after the initial molding and sintering, which is especially costly for ceramic materials [2,3,5]. Besides the time and expense of machining, this step is also limited to simple geometries without overhangs and undercuts. This limits the use of new technologies, like additive manufacturing, which are prone to cracking and failure caused by this shrinkage. While, machining of the ceramic body can be minimized through intelligent mold design that is tailored to the specific sample's dimensional shrinkage [7,8], the amount of shrinkage and wastage can be further reduced through modification to the formulation.

Shrinkage is pronounced for all conventional porous ceramic preparation methods, although it varies strongly with the template used and porosity or pore forming material [9–15]. Established methods to produce macro-porous ceramics include sacrificial templating, direct foaming, replica techniques and partial sintering [1,6,14]. Typical shrinkage values found in the literature are 13–48 vol% for the sacrificial template method [10,12], 56–81 vol% for the thermo-foaming method [9] and 40–72 vol% for the replica method [11,16].

Dittmann et al. [17] introduced a new processing route to produce porous ceramics with a high open porosity using the capillary

suspension phenomenon. Capillary suspensions are three phase systems consisting of a regular suspension and a small amount (< 5 vol%) of a secondary liquid that is immiscible with the primary liquid of the suspension. The secondary liquid forms capillary bridges between the particles and, thus, a sample-spanning network of flocculated particles is formed [18–20]. Upon the creation of this particle network, the suspension becomes gel-like and can be molded, debinded and subsequently sintered to produce porous ceramics with open porosities > 50% and pore sizes in the range of 1 μm to 50 μm that exhibit high mechanical stability and high permeability coefficients [17,21–23]. The advantage of capillary suspension processing over other established methods lies in the fabrication of bodies with porosities above 50% combined with pore sizes less than 10 μm, a combination that is arduous with the aforementioned processing routes [1,6,17,21].

Ceramic capillary suspension precursors are widely applicable as a low cost, environmentally friendly, processing route for macroporous ceramics [17]. These ceramics possess good mechanical properties, and can be tailored in a wide range of porosity and pore size [21]. Maurath et al. [24] already introduced capillary suspension-based inks for 3D printing, which can be used for rapid prototyping and emphasizes the versatility of this processing route. However, the effective productivity must be explicitly studied to establish this new processing route in industry [25,26]. Productivity can be increased by either cost minimization or increased effectiveness, which is related to better quality

* Corresponding author at: KU Leuven, Department of Chemical Engineering, B-3001 Leuven, Belgium.

E-mail address: moritz.weiss@kuleuven.be (M. Weiß).

and more flexibility [7,26]. In this work, we show the effectiveness of ceramic capillary suspensions by investigating forming properties and introduce the applicability for prototyping as well as continuous processing. We examine forming behavior in terms of shrinkage, shape accuracy and green body stability. We show that capillary suspensions feature homogeneous, linear shrinkage, therefore good shape accuracy, and the total shrinkage is reduced by about 10% in comparison to pure suspensions. Furthermore, we combine the capillary suspension approach with a continuous twin-screw extrusion process. Even though we observe air entrainment during extrusion, we present a proof of concept for continuous processing of porous ceramics directly from raw materials through the capillary suspensions processing route.

2. Materials and sample preparation

Capillary suspension pastes were created using alumina particles (α - Al_2O_3) with average particles size of $d_{50,3} = 5.5 \mu\text{m}$ (CT19FG, Almatix GmbH, Ludwigshafen, Germany). The alumina particles have a density of $\rho_{\text{alumina}} = 3.9 \text{ g/cm}^3$ and exhibit an arbitrary isometric shape. Type 4 A zeolite $d_{50,3} = 2.7 \mu\text{m}$ (Sipernat 44MS, Evonik Industries AG, Essen, Germany) was used in the extrusion experiments to prevent damage to the apparatus. The zeolite particles are of uniform cubic shape and have a density of $\rho_{\text{zeolite}} = 2.5 \text{ g/cm}^3$.

Two materials, low viscous paraffin oil (Carl Roth GmbH & Co. KG, dynamic viscosity $\rho_{\text{oil}} = 0.85 \text{ g/cm}^3$, $\eta(20^\circ\text{C}) = 0.03 \text{ Pa s}$) and paraffin wax (Sasolwax 5205, Sasol GmbH, $\rho_{\text{wax}} = 0.78 \text{ g/cm}^3$, $T_{\text{melt}} = 52 - 55^\circ\text{C}$, $\eta(65^\circ\text{C}) = 0.007 \text{ Pa s}$), were used as the bulk phase. As the secondary phase, either an aqueous sucrose solution with 50 vol% D(+)-sucrose (Carl Roth GmbH & Co. KG) or glycerol (Rotipuran, Carl Roth GmbH & Co. KG, $\rho_{\text{g}} = 1.26 \text{ g/cm}^3$, $\eta(65^\circ\text{C}) = 0.06 \text{ Pa s}$) was used. The aqueous sucrose solutions density is $\rho_{\text{suc}} = 0.998 \text{ g/cm}^3$.

The alumina particles were dispersed in the paraffin oil at room temperature using a Hauschild SpeedMixer at 1250 rpm for 2 min and mixed for an additional 2 min at 2000 rpm after adding the sucrose solution. The sample volumes were 40 ml with solid fractions of 15 vol% and 20 vol%. The secondary phase fraction was varied between 0 vol% and 2 vol% (hereafter written as %). The three phase contact angle was measured using the sessile drop method (DataPhysics Instruments GmbH, OCA15, Filderstadt, Germany) on a dense, sintered plate. This system had a contact angle of $66 \pm 1.4^\circ$, placing it in the pendular state [18]. The interfacial tension, measured using the pendant drop method, is $43.1 \pm 0.2 \text{ mN/m}$. The prepared suspensions were molded into a cylindrical form ($r = 5 \text{ mm}$, $h = 3 \text{ mm}$) and placed on an absorbent pad. Samples were demolded directly after spreading and were mechanically debinded on the absorbent pad for 20 days. This extended debinding time was chosen to ensure complete mechanical debinding and steady state values. As shrinkage mainly occurs within the first day and remains constant afterwards a shorter time is generally used in processing, particularly for the pure suspensions, which lose strength after the first day.

For the green body stability and extrusion experiments, a wax-based system using the less abrasive zeolite was employed. Molten wax, 20% zeolite particles and 2% glycerol as secondary liquid were mixed with a high shear dissolver at 1600 rpm for 10 min at $T_{\text{prep}} = 65^\circ\text{C}$ for the premixed extrudates. This system was also in the pendular state with a contact angle, measured at the processing temperature of 65°C , of $87.2 \pm 9.4^\circ$. The interfacial tension is $30.2 \pm 0.7 \text{ mN/m}$. Additionally, extrudates were directly mixed from the raw materials using a co-rotating twin screw extruder ZSK 25 (Coperion GmbH, Stuttgart). Extrusion experiments were performed at the IKT, University of Stuttgart, Stuttgart. We did not perform a mechanical debinding step for the wax-based system. Both the pre-mixed and in situ samples were extruded with a throughput of 2 kg/h at 8 bar and 62°C through a die with inner and outer diameters of 4 mm and 6 mm, respectively. The extrudates were freely cooled prior to debinding and sintering. Sample used for the green body stability measurements were molded into forms

with the dimensions $50 \text{ mm} \times 12 \text{ mm} \times 5 \text{ mm}$ by hand.

All sample were thermally debinded in a debinding oven (Nabertherm LVT 5/11) using a protocol that heated the samples to 200°C (30 min), 500°C (60 min) and then 800°C (15 min) on a porous ceramic plate to completely remove the remaining bulk and secondary phase. The alumina sample were sintered at 1650°C for 2 h and the zeolite sample were sintered at 1100°C for 2 h (Nabertherm LHT 04/17).

2.1. Characterization

Rheological characterization of the suspensions was carried out using a rotational rheometer (Haake Mars II; Thermo Scientific, Karlsruhe, Germany) at 20°C . Yield stress measurements, using a vane geometry (Z20 according to DIN 53019-1), were accomplished using shear stress ramps with a shear stress range from $\sigma = 0.1 - 1000 \text{ Pa}$. Apparent yield stress values were evaluated from deformation vs. stress curves using the tangent method.

Information about the green body stability was obtained from visual inspection of wax-based samples placed on two metal bars of 8 mm height, separated by 4 cm, and heating the samples to 100°C in an oven for 75 min.

A 3D laser scanning confocal microscope (Keyence VK-X100) was used to measure the sample dimensions during processing. Two perpendicular sections were recorded and the total volume was calculated assuming that the samples were truncated cones (conical frustum) using Matlab. Circles were fit to the top and bottom perpendicular sections at the average heights h_{mean} and at $0.1 \cdot h_{\text{mean}}$ to find the true, extrapolated cone volume. We measured the bottom radius at $0.1 \cdot h_{\text{mean}}$ to avoid fitting problems caused by noisy data near the reflective substrate. Some samples show strong edge super-elevation, which we did not consider in the average height calculation, but which was added to the calculated cylinder volume. The method was developed in accordance to the slumping test, commonly used for evaluating cementitious paste workability [27]. While the slump test uses cone geometries as molds to observe concretes slumping per time [27], we used cylindrical molds to facilitate homogeneous shrinkage. Shape accuracy was determined from scanned sample cross sections.

Shrinkage of the sintered sample was calculated using the ratio of volumes from porosity ε , dry mass m_{dry} and the form volume V_{form} according to:

$$\frac{V}{V_{\text{form}}} = \frac{m_{\text{dry}}}{\rho \cdot (1 - \varepsilon) \cdot V_{\text{form}}} \quad (1)$$

The porosity was determined using Archimedes' principle according to DIN EN 993-1. Scanning-electron-microscope (SEM) micrographs (S-4500; Hitachi High-Technologies Europe GmbH) of sintered part cross-sections were used to analyze the microstructure. Pore sizes were calculated via the Line-Intercept-Method [28].

3. Results and discussion

3.1. Green body stability

As previously shown for alumina-based and other capillary suspensions [21,29–31], we observed an increase in yield stress with increasing amounts of secondary phase in the pendular state as the size of the capillary bridges and their number increases, and then a peak and subsequent reduction in the yield stress as the bridges coalesce in the funicular state, as shown in Fig. 1. The capillary suspension with $\phi_{\text{sec}} = 2\%$ shows highest yield stress (Fig. 1A) and best green body stability (Fig. 1B). With the exception of 2% and 3%, the other samples failed under their own weight after 75 min. The capillary suspension samples did not fail catastrophically, although they did deform slightly. The green body stability is related to the paste yield stress, with the samples having $\sigma_{\text{yield}} \geq 250 \text{ Pa}$ able to withstand this test. This increased

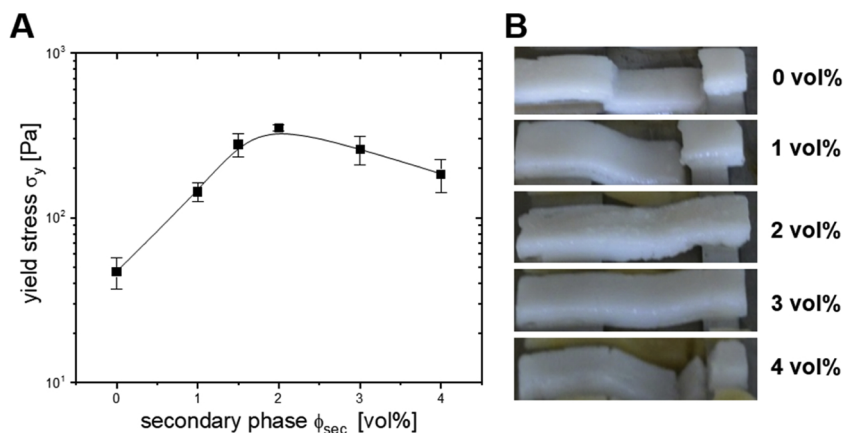


Fig. 1. (A) Paste yield stress versus secondary phase volume fraction for the wax-based zeolite system ($\phi_{solid} = 0.15$). (B) Images showing wax-based samples of the pastes lying on two bars after heating to 100 °C for 75 min. Their deformation behavior presents the green body stability.

green body stability will enable formation of complex forms, e.g. overhangs or undercuts can be retained.

3.2. Shape-accuracy and shrinkage

While the green body stability is a good indicator for the applicability of these pastes, the shrinkage and shape accuracy during debinding and sintering must also be measured. We performed laser microscopic measurements of the cylindrical alumina-based samples to determine shrinkage and shape accuracy after mechanical and thermal debinding as well as in the sintered state. Fig. 2 shows 3D laser microscopic images (top) as well as cross sections (bottom) of a pure and a

capillary suspension after debinding. The pure suspension (left) has superelevations on the top surface edges and clear edge exaggerations on the bottom surface indicating either spreading or asymmetric shrinkage. The higher superlevation on one side of the pure suspension probably results from inaccuracies during demolding as well as a shearing failure. Additionally, a significant difference between the top and bottom radii is observed. On the contrary, the capillary suspension (right) shows a good shape accuracy with clean edges on the top surface and very little slumping or spreading at the bottom and almost perfectly straight edges from bottom to top. Bitsch et al. [32] showed similar results for the edge contour of wet electrode slurries. The volume of the largest inscribing disk, that is the largest disk that could be cut from the

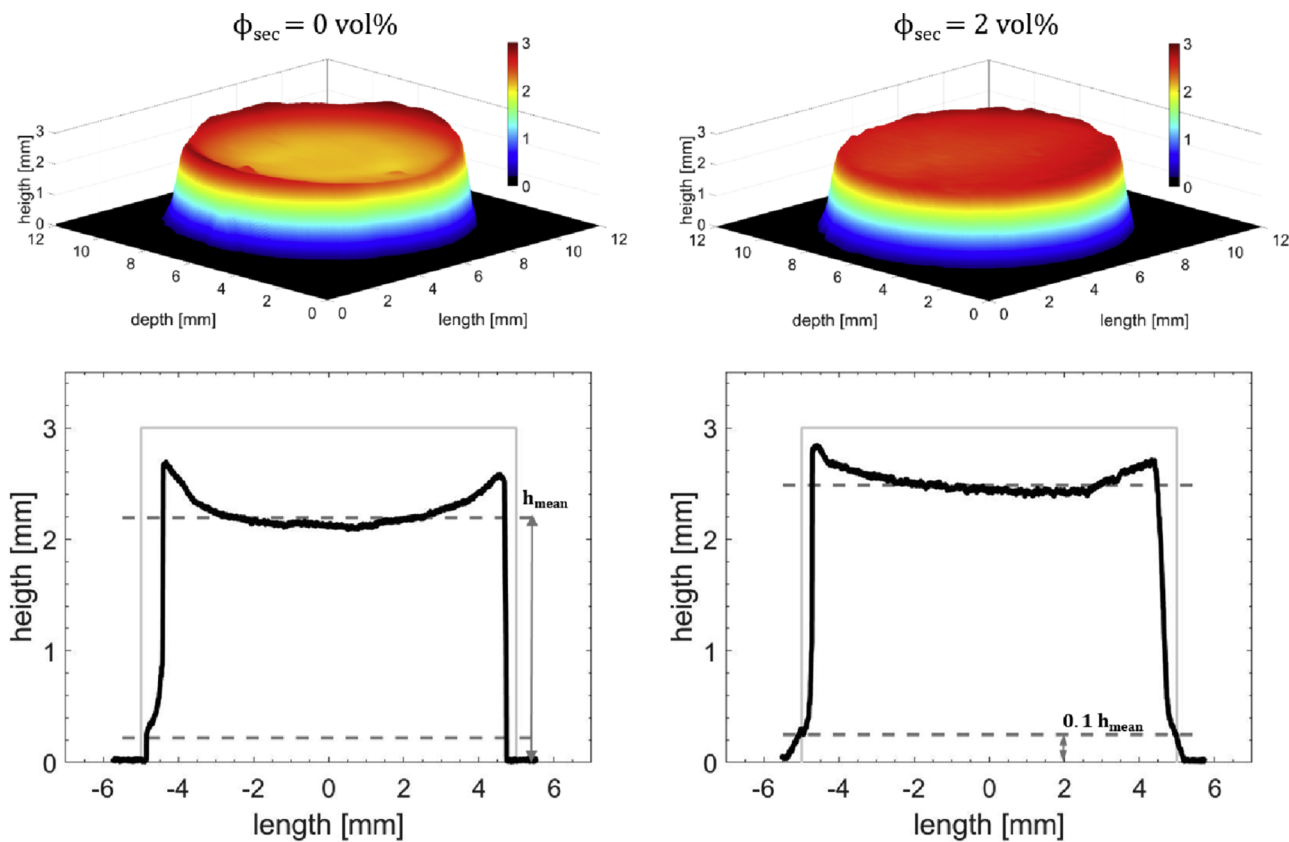


Fig. 2. (Top) 3D-laser microscopic images and (bottom) the corresponding cross section of mechanically debinded alumina-based ($\phi_{solid} = 20$ vol%) systems. The pure suspension is illustrated on the left, the capillary suspension with $\phi_{sec} = 2$ vol% on the right. Samples were molded in a cylindrical form ($r_{form} = 5$ mm, $h_{form} = 3$ mm), as shown by the grey lines.

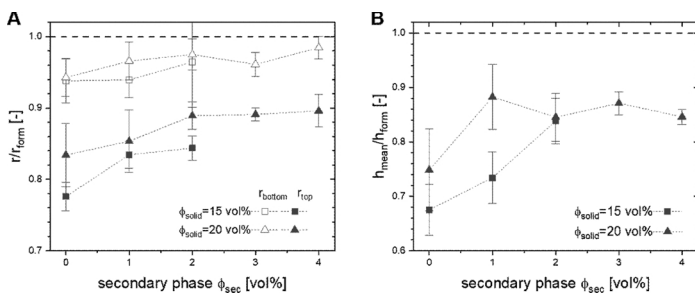


Fig. 3. Normalized linear shrinkage data of the thermal debinded oil-based alumina systems. The samples were molded in a cylindrical form ($r_{\text{form}} = 5 \text{ mm}$, $h_{\text{form}} = 3 \text{ mm}$), mechanically debinded on an absorbent pad for 20 days, followed by a thermal debinding procedure up to $800 \text{ }^\circ\text{C}$ for 15 min. (A) Top and bottom radii, measured at h_{mean} and $0.1 \cdot h_{\text{mean}}$, respectively, normalized by form radius r_{form} and (B) mean height normalized by the form height versus secondary phase volume fraction. The dashed lines represent the form dimensions at a ratio of one.

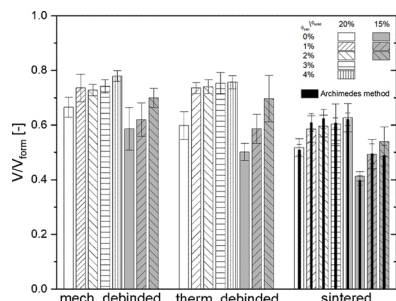


Fig. 4. Shrinkage of different sample compositions for the three preparation states (after mechanical debinding, thermal debinding and sintering). The solid volume fraction is $\phi_{\text{solid}} = 20 \text{ vol}\%$ for the white bars and the secondary phase fraction varies from $\phi_{\text{sec}} = 0\text{--}4 \text{ vol}\%$. Grey bars represent samples with a solid content of $\phi_{\text{solid}} = 15 \text{ vol}\%$ and secondary phases from $\phi_{\text{sec}} = 0\text{--}2 \text{ vol}\%$.

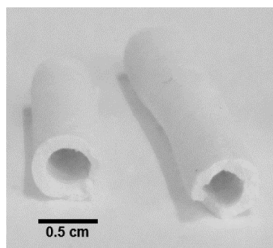


Fig. 5. Fractured segment of a sintered hollow tube based on an extruded capillary suspension from zeolite particles. This sample ($\phi_{\text{solid}} = 20 \text{ vol}\%$, $\phi_{\text{sec}} = 2 \text{ vol}\%$) was mixed in situ prior to extrusion.

debinded form, relative to the form's volume is only 0.57 for the pure suspension and 0.65 for the capillary suspension. Therefore, the capillary suspension offers higher shape accuracy, which enables complex shapes to be produced with less finishing work and less waste, but it does undergo shrinkage during mechanical debinding.

To further evaluate our findings, we determined the linear shrinkage by measuring the bottom and top radii as well as the mean sample height from the cross sectional images (Fig. 2). The results for the alumina samples with $\phi_{\text{solid}} = 15\%$ and $\phi_{\text{solid}} = 20\%$ after thermal debinding are shown in Fig. 3. Fig. 3A shows the normalized radii shrinkage for different amounts of secondary phase. The bottom radius shape accuracy $r_{\text{bottom}}/r_{\text{form}}$ is independent of the amount of secondary phase, while the linear top shape accuracy is increased for capillary suspension until $\phi_{\text{sec}} = 2\%$ after which it remains constant. For

$\phi_{\text{solid}} = 20\%$ shape accuracy increases from 0.83 ± 0.04 for pure suspensions to 0.89 ± 0.02 for capillary suspensions. For lower solid fractions of $\phi_{\text{solid}} = 15\%$ $r_{\text{top}}/r_{\text{form}}$ rises from 0.78 ± 0.02 to 0.84 ± 0.02 when forming a capillary suspension. For solid fractions of $\phi_{\text{solid}} = 20\%$ and insufficient amounts of secondary phase to build a sample spanning network, the measured standard deviation is twice as high as for capillary suspensions. As mentioned earlier, the high deviations probably result from inaccuracies during demolding as well as from shearing failure. The bottom shrinkage is mainly controlled by the substrate adhesion, whereas the top shrinkage is dominated by particle mobility and orientation [33,34]. The strong decrease in shrinkage of the top while the bottom remains uniform means a substantially lower difference between the top and bottom radii and, therefore, an increasing shape accuracy. These findings are in good agreement with the images shown in Fig. 2. Besides the substrate adhesion, the capillary suspension's bottom shrinkage can be linked to its increased yield stress while the pure suspension's bottom radius shape accuracy seems to be due to stronger edge exaggerations.

The normalized linear height shrinkage for different secondary phase fractions is shown in Fig. 3B. For the samples with $\phi_{\text{solid}} = 15\%$, the pure suspension green body height is only 68% of the form height while the capillary suspension ($\phi_{\text{sec}} = 2\%$) height is still 84% of the initial height. As mentioned before, the top radius of the pure suspension is smaller than for the capillary suspension. Therefore, this increase of the mean height for capillary suspensions is even more remarkable with respect to the resulting volumetric shape accuracy. The capillary suspension with $\phi_{\text{solid}} = 20\%$ shows constant shrinkage in height and radii for $\phi_{\text{sec}} = 2\text{--}4\%$, as well as good reproducibility as indicated by the small error bars. This plateau area is correlated to the suspension yield stress peak (Fig. 1A and Dittmann et al. [21]). Capillary suspensions are, in comparison to pure suspensions, better in terms of their shape accuracy in all geometric dimensions.

The shrinkage in all three states, mechanically debinded, thermal debinded and sintered was analyzed from laser microscopic data and is shown in Fig. 4. The black bars in the sintered state represent the shrinkage additionally determined from Archimedes method order to confirm the laser microscopic data. The results of the two methods are in good agreement for all eight measured samples. This non-invasive laser microscopic method facilitates the determination of the sample's volume regardless of its state.

The graph in Fig. 4 shows a strong decrease in shrinkage for capillary suspensions in comparison to pure suspensions. The slight differences between mechanical and thermal debinded sample shrinkage indicates that the greatest change to the network structure occurs as the

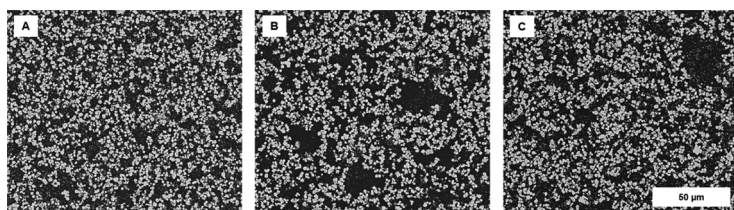


Fig. 6. SEM (BSE) crosscut images of sintered capillary suspensions using paraffin wax as bulk phase, $\phi_{\text{solid}} = 20 \text{ vol}\%$ zeolite particles and $\phi_{\text{sec}} = 2 \text{ vol}\%$ glycerol as secondary phase, with constant sintering conditions ($T_{\text{sinter}} = 1100 \text{ }^\circ\text{C}$, $t_{\text{sinter}} = 2 \text{ h}$). Solid particles appear as light grey and pores as black. (A) laboratory molded, $\epsilon = 67\%$, $d_{\text{pore}} = 7.8 \text{ }\mu\text{m}$, (B) premixed extruded, $\epsilon = 71\%$, $d_{\text{pore}} = 17.6 \text{ }\mu\text{m}$, (C) directly mixed, extruded, $\epsilon = 71\%$, $d_{\text{pore}} = 17.1 \text{ }\mu\text{m}$.

main part of bulk phase is absorbed into the pad and, therefore, the thermal debinding does not affect the resulting porosity. Removal of the bulk phase during mechanical debinding occurs quickly, within the first day, as evidenced by monitoring shrinkage during this step. Therefore, a debinding time greater than 24 h at room temperature is unnecessary. Indeed, the wax-based systems used for extrusion in this paper or 3D-printing of capillary suspensions [24], samples were thermally debinded without mechanical debinding. For these samples, the thermal debinded state indicates the maximum sample porosity which can be reached by this composition if we sinter for a minimum of time. For a particle fraction of $\phi_{\text{solid}} = 20\%$, the maximum porosity is 5% higher for the capillary ($V_2 = 2\%$) than for the pure suspension with the maximum porosity even 10% higher for the $\phi_{\text{solid}} = 15\%$ sample. Again, the capillary suspension ($\phi_{\text{solid}} = 20\%$) form a plateau area for secondary phase fractions of $\phi_{\text{sec}} = 2\text{--}4\%$. Dittmann et al. previously showed that capillary suspension derived ceramics are tunable in this region. While the porosity stays constant, the pore size distribution varies with the secondary phase fraction [21].

A more homogeneous shrinkage between the top and the bottom is not only consistent with a better shape accuracy but also with a more homogeneous drying stress within the suspension [35]. This is consistent with the results of Schneider et al. [34] where cracking was reduced. This confirms our previous results and emphasizes the benefits of capillary suspensions in terms of shape accuracy, molding behavior and defect-free drying. This combination is particularly interesting for additive manufacturing processes.

3.3. Extrusion

The cold-extrusion of ceramic capillary suspensions is possible and can even be used to form complex shapes such as hollow tubes, as shown in Fig. 5. We successfully extruded premixed capillary suspensions as well as directly mixed capillary suspensions from raw materials with a twin screw extruder. None of the resulting extrudates cracked and they all showed homogeneous shrinkage behavior during debinding and sintering.

Fig. 6 shows cross-cut images of a laboratory molded capillary suspension (Fig. 6A), an extruded, premixed (Fig. 6B) and an extruded, directly mixed capillary suspension (Fig. 6C). The molded capillary suspension shows the typical homogenous pore structure with a porosity of $\varepsilon = 67\%$ and an average pore size of $d_{\text{pore}} = 7.8 \mu\text{m}$. The porosities of both extruded samples are between $70\% < \varepsilon < 75\%$, the average pore size for the extruded premixed and extruded directly mixed sample is $17.6 \mu\text{m}$ and $17.1 \mu\text{m}$, respectively. This difference in porosity and pore size between the extruded and the laboratory molded sample corresponds to the microstructural inhomogeneity caused by the entrainment of air during extrusion. Air entrainment is a common issue in extrusion processing [36–42], which can be solved by an appropriate screw concept, barrel fill length or vacuum extrusion [36,40,42] in further experiments. As seen from the SEM-images, and further proven by μCT analysis of the extruded green bodies, there is no observable difference between the two extruded samples. Therefore, capillary suspensions can be mixed and formed from raw materials in a single, continuous process. Such continuous processing will enable this method to be easily applied to existing high throughput industrial operations.

4. Conclusion

In this paper, we investigated processing behavior of ceramic capillary suspension precursors comprising shrinkage, shape accuracy, green body stability and showed their suitability for a continuous extrusion process. Capillary suspensions offer higher green body stabilities than pure suspensions caused by their increased yield stress. Using a confocal laser scanning microscope, we investigated the shrinkage and shape accuracy in all three stages: mechanically debinded,

thermally debinded and sintered. The substrate adhesion is the dominant mechanism on the bottom and prevents shrinkage, therefore, we did not observe a difference between pure and capillary suspensions in the shrinkage at the bottom. Linear top shrinkage, the free surface, is significantly reduced through the capillary suspension approach. We observed an increase of up to 7% of top radius net-shape accuracy for capillary suspensions in comparison to pure suspensions, thus the linear difference from bottom to top is only about 12% for the capillary suspension and 16% for the corresponding pure suspension. Furthermore, the capillary suspension's height is increased by 16% compared to pure suspensions. For total volumetric shape accuracy, this means an increase from 0.5 for the pure suspension to 0.7 for capillary suspensions relative to the form's volume.

Capillary suspensions combine green body stability and high shape accuracy with low and nearly uniform shrinkage, which enables more accurate molds to be designed and the final machining to be reduced. On this basis, we performed extrusion experiments using a twin-screw extruder and succeeded in forming the capillary suspensions from the raw components without any difference from the premixed, extruded capillary suspensions. The premixed, as well as the directly mixed extruded bodies' microstructures show inhomogeneities that result from air entrainments. However, our experiments show that extruding and sintering complex structures from ceramic capillary suspension precursors result in crack-free bodies and, therefore, can be applied for continuous shaping processes.

Ceramic capillary suspension precursors are widely applicable as a low cost, environmentally friendly, processing route for macroporous ceramics [17]. By this concept, ceramics can be tailored in a wide range of porosity and pore size, offering good mechanical properties [21]. The forming properties, green body stability, shape accuracy and shrinkage shown here, combined with the ability of capillary suspensions to suppress crack formation demonstrate the method's suitability for industrial and laboratory use. Sintered body dimensions can be calculated and accurately realized through simple engineered mold design. More complex bodies can be realized by 3D-printing processes, e.g. honeycombs with high specific strength or prototyping [24], as well as in continuous processes like the presented extrusion. Therefore, this work emphasizes the strengths of ceramic capillary suspension route as an accurate, low cost, widely applicable variable fabrication method for porous ceramics. We anticipate possible application in various fields, like membranes or filters [34], lightweight construction materials [24], biomedical devices, gas diffusers, thermal insulators or catalyst carriers.

Acknowledgements

The authors would like to thank Almatix GmbH and Evonik Industries AG for the donation of the alumina, the zeolite particles and the smooth collaboration. Christian Bonten for access to his extruder and Benjamino R. Formisano for contributing to the extrusion experiments. Felix Braun for contributing to the green body stability and extrusion experiments. Finally we acknowledge financial support from the European Research Council under the European Union's Seventh Framework Program (FP/2007-2013)/ERC grant agreement no. 335380 and support from the Research Foundation Flanders (FWO) Odysseus Program (grant agreement no. G0H9518N).

References

- [1] T. Ohji, M. Fukushima, Macro-porous ceramics: processing and properties, *Int. Mater. Rev.* 57 (2012) 115–131, <https://doi.org/10.1179/1743280411Y.0000000006>.
- [2] P. Greil, Near net shape manufacturing of ceramics, *Mater. Chem. Phys.* 61 (1999) 64–68, [https://doi.org/10.1016/S0254-0584\(99\)00115-7](https://doi.org/10.1016/S0254-0584(99)00115-7).
- [3] B. Carter, G. Norton, *Ceram. Mater. Sci. Eng.* (2007), <https://doi.org/10.1007/978-0-387-46271-4>.
- [4] J.C. Venkata Reddy Nallagundla, X.Hu Rakesh Lingam, E.M. Wouterson, M. Liu, *Handbook of Manufacturing Engineering and Technology*, (2015), <https://doi.org/10.1007/978-1-4471-4670-4>.

- [5] A. Zocca, P. Colombo, C.M. Gomes, J. Günster, Additive manufacturing of ceramics: issues, potentialities, and opportunities, *J. Am. Ceram. Soc.* 98 (2015) 1983–2001, <https://doi.org/10.1111/jace.13700>.
- [6] A.R. Studart, U.T. Gonzenbach, E. Tervoort, L.J. Gauckler, Processing routes to macroporous ceramics: a review, *J. Am. Ceram. Soc.* 89 (2006) 1771–1789, <https://doi.org/10.1111/j.1551-2916.2006.01044.x>.
- [7] R.-S. Lee, Y.-M. Chen, C.-Z. Lee, Development of a concurrent mold design system: a knowledge-based approach, *Comput. Integr. Manuf. Syst.* 10 (1997) 287–307, [https://doi.org/10.1016/S0951-5240\(97\)00021-9](https://doi.org/10.1016/S0951-5240(97)00021-9).
- [8] R.M. German, K.F. Hens, Key issues in powder injection-molding, *Ceram. Am. Bull. Soc.* 70 (1991) 1294–1302.
- [9] S. Vijayan, R. Narasimman, C. Prudvi, K. Prabhakaran, Preparation of alumina foams by the thermo-foaming of powder dispersions in molten sucrose, *J. Eur. Ceram. Soc.* 34 (2014) 425–433, <https://doi.org/10.1016/j.jeurceramsoc.2013.08.023>.
- [10] J. Cao, C.R. Rambo, H. Sieber, Manufacturing of microcellular, biomorphous oxide ceramics from native pine wood, *Ceram. Int.* 30 (2004) 1967–1970, <https://doi.org/10.1016/j.ceramint.2003.12.181>.
- [11] K. Prabhakaran, A. Melkeri, N.M. Gokhale, S.C. Sharma, Preparation of macroporous alumina ceramics using wheat particles as gelling and pore forming agent, *Ceram. Int.* 33 (2007) 77–81, <https://doi.org/10.1016/j.ceramint.2005.07.020>.
- [12] K. Prabhakaran, N.M. Gokhale, S.C. Sharma, R. Lal, A novel process for low-density alumina foams, *J. Am. Ceram. Soc.* 88 (2005) 2600–2603, <https://doi.org/10.1111/j.1551-2916.2005.00446.x>.
- [13] U.T. Gonzenbach, A.R. Studart, D. Steinlin, E. Tervoort, L.J. Gauckler, Processing of particle-stabilized wet foams into porous ceramics, *J. Am. Ceram. Soc.* 90 (2007) 3407–3414, <https://doi.org/10.1111/j.1551-2916.2007.01907.x>.
- [14] I. Akartuna, A.R. Studart, E. Tervoort, L.J. Gauckler, Macroporous ceramics from particle-stabilized emulsions, *Adv. Mater.* 20 (2008) 4714–4718, <https://doi.org/10.1002/adma.200801888>.
- [15] J. Cao, C.R. Rambo, H. Sieber, Preparation of porous Al₂O₃-ceramics by biotemplating of wood, *J. Porous Mater.* 11 (2004) 163–172, <https://doi.org/10.1023/B:JOPO.0000038012.58705.c9>.
- [16] Y. Hotta, P.C.A. Alberius, L. Bergström, Coated polystyrene particles as templates for ordered macroporous silica structures with controlled wall thickness, *J. Mater. Chem.* 13 (2003) 496–501, <https://doi.org/10.1039/b208795m>.
- [17] J. Dittmann, E. Koos, N. Willenbacher, Ceramic capillary suspensions: novel processing route for macroporous ceramic materials, *J. Am. Ceram. Soc.* 96 (2013) 391–397, <https://doi.org/10.1111/jace.12126>.
- [18] E. Koos, N. Willenbacher, Capillary forces in suspension rheology, *Science (80-)* 331 (2011) 897–900.
- [19] E. Koos, Capillary suspensions: particle networks formed through the capillary force, *Curr. Opin. Colloid Interface Sci.* 19 (2014) 575–584, <https://doi.org/10.1016/j.cocis.2014.10.004>.
- [20] F. Bossler, E. Koos, Structure of particle networks in capillary suspensions with wetting and nonwetting fluids, *Langmuir* 32 (2016) 1489–1501, <https://doi.org/10.1021/acs.langmuir.5b04246>.
- [21] J. Dittmann, N. Willenbacher, Micro structural investigations and mechanical properties of macro porous ceramic materials from capillary suspensions, *J. Am. Ceram. Soc.* 97 (2014) 3787–3792, <https://doi.org/10.1111/jace.13184>.
- [22] J. Dittmann, J. Maurath, B. Bitsch, N. Willenbacher, Highly porous materials with unique mechanical properties from smart capillary suspensions, *Adv. Mater.* 28 (2016) 1689–1696, <https://doi.org/10.1002/adma.201504910>.
- [23] J. Maurath, J. Dittmann, N. Schultz, N. Willenbacher, Fabrication of highly porous glass filters using capillary suspension processing, *Sep. Purif. Technol.* 149 (2015) 470–478, <https://doi.org/10.1016/j.seppur.2015.06.022>.
- [24] J. Maurath, N. Willenbacher, 3D printing of open-porous cellular ceramics with high specific strength, *J. Eur. Ceram. Soc.* 37 (2017) 4833–4842, <https://doi.org/10.1016/j.jeurceramsoc.2017.06.001>.
- [25] N. Becheikh, R. Landry, N. Amara, Lessons from innovation empirical studies in the manufacturing sector: a systematic review of the literature from 1993–2003, *Technovation* 26 (2006) 644–664, <https://doi.org/10.1016/j.technovation.2005.06.016>.
- [26] S. Tangen, Demystifying productivity and performance, *Int. J. Product. Perform. Manag.* 54 (2005) 34–46, <https://doi.org/10.1108/17410400510571437>.
- [27] Z. Tan, S.A. Bernal, J.L. Provis, Reproducible mini-slump test procedure for measuring the yield stress of cementitious pastes, *Mater. Struct. Constr.* 50 (2017) 1–12, <https://doi.org/10.1617/s11527-017-1103-x>.
- [28] J.C. Russ, R.T. Dehoff, *Practical Stereology*, Springer Science & Business Media, 2012.
- [29] F. Bossler, J. Maurath, K. Dyhr, N. Willenbacher, E. Koos, Fractal approaches to characterize the structure of capillary suspensions using rheology and confocal microscopy, *J. Rheol. (N. Y. N. Y.)* 62 (2018) 183–196, <https://doi.org/10.1122/1.4997889>.
- [30] S.J. Heidlebaugh, T. Domenech, S.V. Iasella, S.S. Velankar, Aggregation and separation in ternary particle/oil/water systems with fully wettable particles, *Langmuir* (2014), <https://doi.org/10.1021/la4039396>.
- [31] S.S. Velankar, A non-equilibrium state diagram for liquid/fluid/particle mixtures, *Soft Matter* 11 (2015) 8393–8403, <https://doi.org/10.1039/C5SM01901J>.
- [32] B. Bitsch, J. Dittmann, M. Schmitt, P. Scharfer, W. Schabel, N. Willenbacher, A novel slurry concept for the fabrication of lithium-ion battery electrodes with beneficial properties, *J. Power Sources* 265 (2014) 81–90, <https://doi.org/10.1016/j.jpowsour.2014.04.115>.
- [33] E. Cohen, E. Gutoff, E.D. Cohen (Ed.), *Modern Coating and Drying Technology*, VCH Verlagsgesellschaft, Weinheim, 1992, pp. 267–296 <http://swb.bsz-bw.de/DB=2.1/PPN?PPN=029207401>.
- [34] M. Schneider, J. Maurath, S.B. Fischer, M. Weiß, N. Willenbacher, E. Koos, Suppressing crack formation in particulate systems by utilizing capillary forces, *ACS Appl. Mater. Interfaces* 9 (2017) 11095–11105, <https://doi.org/10.1021/acsami.6b13624>.
- [35] G.W. Scherer, Theory of drying, *J. Am. Ceram. Soc.* 73 (1990) 3–14, <https://doi.org/10.1111/j.1151-2916.1990.tb05082.x>.
- [36] F.H. Cisneros, J.L. Kokini, A generalized theory linking barrel fill length and air bubble entrapment during extrusion of starch, *J. Food Eng.* 51 (2002) 139–149, [https://doi.org/10.1016/S0260-8774\(01\)00050-4](https://doi.org/10.1016/S0260-8774(01)00050-4).
- [37] C.S. Lai, J. Guetzlaff, R.C. Hosney, *Role of Sodium Bicarbonate and Trapped Air in Extrusion*, (1989).
- [38] T. Liu, Minimum wet thickness coating in extrusion, *Chem. Eng.* 47 (1992) 1703–1713.
- [39] Y. Shao, J. Qiu, S.P. Shah, Microstructure of extruded cement-bonded fiberboard, *Cem. Concr. Res.* 31 (2001) 1153–1161, [https://doi.org/10.1016/S0008-8846\(01\)00535-X](https://doi.org/10.1016/S0008-8846(01)00535-X).
- [40] F. Händle, *Extrusion in Ceramics*, Springer Science & Business Media, 2007, <https://doi.org/10.1007/978-3-540-27102-4>.
- [41] J.L. White, *Twin Screw Extrusion: Technology and Principles*, (1991) <https://books.google.com/books?id=nbViGwAACAAJ&pgis=1>.
- [42] N.E.M. del Pilar, C. Rauwendaal, *Troubleshooting the Extrusion Process*, (2001).